To appear in the *Journal of Geophysical Research*, 2000.

# Mars Global Surveyor Thermal Emission Spectrometer (TES) observations of dust opacity during aerobraking and science phasing

Michael D. Smith and John C. Pearl
NASA Goddard Space Flight Center, Greenbelt, Maryland

Barney J. Conrath
Center for Radiophysics and Space Research, Cornell University, Ithaca, New York

Philip R. Christensen
Department of Geology, Arizona State University, Tempe

## Abstract

The Mars Global Surveyor (MGS) arrived at Mars in September 1997 near Mars's southern spring equinox and has now provided monitoring of conditions in the Mars atmosphere for more than half a Mars year. The large majority of the spectra taken by the Thermal Emission Spectrometer (TES) are in a nadir geometry (downward looking mode) where Mars is observed through the atmosphere. Most of these contain the distinct spectral signature of atmospheric dust. For these nadir-geometry spectra we retrieve column-integrated infrared aerosol (dust) opacities. TES observations during the aerobraking and science-phasing portions of the MGS mission cover the seasonal range $L_s$=184°–28°. Excellent spatial coverage was obtained in the southern hemisphere. Northern hemisphere coverage is generally limited to narrow strips taken during the periapsis pass but is still very valuable. At the beginning of the mission the 9-$\mu$m dust opacity at midsouthern latitudes was low (0.15–0.25). As the season advanced through southern spring and into summer, TES observed several regional dust storms (including the Noachis dust storm of November 1997) where peak 9-$\mu$m dust opacities approached or exceeded unity, as well as numerous smaller local storms. Both large and small dust storms exhibited significant changes in both spatial coverage and intensity over a timescale of a day. Throughout southern spring and summer the region at the edge of the retreating southern seasonal polar ice cap was observed to be consistently more dusty than other latitudes.

## 1. Introduction

Dust aerosols are always present in the Mars atmosphere. Their presence significantly effects the thermal structure of the atmosphere and is a major driver of atmospheric circulations at all spatial scales. A long history of both Earth-based and spacecraft-based observation exists of dust in the Mars atmosphere. Earth-based observations of Martian dust date back at least to the 1870s with the work of Schiaparelli. *Martin and Zurek* [1993] give a good review of the history of Earth-based (and spacecraft-based) dust cloud observations. More recently, images from the Hubble Space Telescope [e.g., *James et al.*, 1997; *Wolff et al.*, 1997] and observations from amateur astronomers [*Beish and Parker*, 1990] have helped to characterize the frequency and location of dust storms. Although clouds of dust can be easily identified in images of Mars, it is very difficult to accurately estimate a column-integrated opacity.

Spacecraft observation of Mars has allowed a more quantitative analysis of dust opacity. Data from the infrared spectrometer carried by Mariner 6 and 7 clearly show the signature of dust at 900–1200 $cm^{-1}$ (8–11 $\mu$m) [*Horn et al.*, 1972; *Cimino and Calvin*, 1996]. Combined with an estimate for atmospheric and surface temperatures, these data can be used to compute column-integrated dust opacity using radiative transfer techniques. Mariner 9 also carried an infrared spectrometer [*Hanel et al.*, 1972a] and monitored the decay of the global dust storm of 1971 [*Hanel et al.*, 1972b; *Toon and Pollack*, 1977]. Dust opacities have recently been derived from these data by *Santee and Crisp* [1993] and by *Fenton et al.* [1997]. The two Viking orbiters did not carry infrared spectrometers, but data from the broadband infrared thermal mapper (IRTM) [*Chase et al.*, 1978] can be used to accurately retrieve dust opacity and have proven to be very useful for monitoring dust opacities and local dust storms during the Viking mission [*Martin*, 1986; *Martin and Richardson*, 1993; *Peterfreund*, 1985]. Observations of the Sun by the Viking lander give dust opacity at visible wavelengths [*Pollack et al.*, 1979; *Colburn et al.*, 1989]. Thermal infrared spectra recorded using ground-based telescopes [*Pollack et al.*, 1990] and the Kuiper Airborne Observatory [*Roush et al.*, 1995] have also been used to estimate dust opacities. Most recently, the Pathfinder lander has used observations of the Sun during the day and of bright stars at night to obtain dust opacity [*Smith et al.*, 1997; *Smith and Lemmon*, 1999].

In this paper we extend this baseline of observations by reporting results of the retrieval of column-integrated dust opacity using infrared spectra taken by the Thermal Emission Spectrometer (TES) onboard the Mars Global Surveyor (MGS). At least two other instruments on MGS can also provide useful information on dust opacities. The Mars Observer Camera (MOC) imaged the large regional dust storm in Noachis Terra, as well as numerous other smaller storms [e.g., *Malin et al.*, 1998a; *Malin*, 1998], and *Toigo et al.* [1998] have used an analysis of shadows in MOC images to estimate visible dust opacities. *Ivanov and Muhleman* [1998] have used data from the Mars Orbiter Laser Altimeter (MOLA) to infer dust opacity from measurements of atmospheric transmittance.

We next review the characteristics of the TES instrument and its observations in section 2. In section 3 we describe the retrieval algorithm used to obtain column-integrated dust opacities. In section 4 we present results and compare them with results from previous spacecraft missions. Finally, we summarize our findings in section 5.

## 2. Data Set

### 2.1. TES Instrument

The Thermal Emission Spectrometer (TES) is a thermal infrared interferometer/ spectrometer with additional broadband visible and thermal channels [*Christensen et al.*, 1992]. Six detectors in a three-by-two array simultaneously take spectra covering the spectral range from 200 to 1600 $cm^{-1}$ (6–50 $\mu$m), with a selectable sampling of either 5 or 10 $cm^{-1}$ (a large majority of the data collected so far has 10-$cm^{-1}$ sampling). A pointing mirror allows TES to view from nadir to above both the forward and aft limbs, where the atmosphere is observed without direct contribution from the surface. Each pixel subtends a 8.3-mrad field of view. The highly eccentric orbit of MGS during the period of observations considered here causes highly variable spatial resolution for TES observations, ranging from 10 km (including smear caused by spacecraft motion) near periapsis to several hundred kilometers near apoapsis.

Figure 1 shows examples of typical daytime TES spectra. Spectra are shown here in terms of their equivalent brightness temperature to emphasize features. The $CO_2$ gas absorption centered at 667 $cm^{-1}$ (15 $\mu$m) is used to retrieve atmospheric temperatures [see *Conrath et al.*, this issue]. The spectral signa-

tures of dust and $H_2O$ ice aerosols are clearly visible and are distinct from each other and from the 15-$\mu$m $CO_2$ band. Dust has a broad peak centered at 1075 $cm^{-1}$ and nonnegligible absorption throughout the entire spectrum except near 1300 $cm^{-1}$. Absorption from $H_2O$ ice has a broad peak near 825 $cm^{-1}$ and a sharper peak at 229 $cm^{-1}$ (only hinted at in Figure 1) and is small for wavenumbers > 1000 $cm^{-1}$ [see *Curran et al.*, 1973; J. C. Pearl, Mars water ice clouds: Observations by the Thermal Emission Spectrometer (TES) during the first Martian year, submitted to *Journal of Geophysical Research*, 1999]. The most transparent part of the spectrum is near 1300 $cm^{-1}$.

### 2.2. Mars Global Surveyor Orbit Characteristics

The Mars Global Surveyor (MGS) entered into orbit around Mars in September 1997 and performed over 200 orbits of aerobraking before entering a parking, or "science-phasing," orbit in March 1998. Mars Global Surveyor remained in the science-phasing orbit until September 1998, when aerobraking to the final mapping orbit resumed. A brief summary of the first part of the mission is given by *Albee et al.* [1998].

The initial orbital period of MGS was ~45 hours. During the first period of aerobraking (September 1997 to March 1998) the orbital period was gradually decreased to 11.6 hours, the latitude of periapsis moved from 32°N to 51°N, and the local time of periapsis changed from 1820 hours to 1220 hours. There was no aerobraking attempted during the science-phasing orbit, and so the orbital period remained at 11.6 hours. The latitude of periapsis continued migrating northward from 51°N going over the north pole and reaching 61°N at the end of the science-phasing observations. Local time of periapsis was near dawn at the beginning of science phasing and then near dusk after periapsis moved over the north pole.

### 2.3. Observations During Aerobraking and Science Phasing

Because of the elliptical nature of the MGS orbit, observations from TES fall into two main categories: those taken during the periapsis pass and those taken during the rest of the orbit (the "apoapsis portion" of the orbit). Observations were split fairly evenly between the two categories during aerobraking when the orbital period was long. Data playback was limited during the science-phasing portion of the mission, and the majority of observations were focused on the periapsis pass.

For any one orbit the periapsis pass gives one narrow (three-pixel-wide) strip of observations running roughly north to south. Coverage was primarily in the northern hemisphere and was usually in daylight. During the apoapsis portion of the orbit the spacecraft was placed into a roll configuration so that by using the TES pointing mirror, most or all of the disk of Mars could be imaged once per 100 min. This allowed large portions of the southern hemisphere to be sampled, although more than half of the spectra were taken on the nighttime portion of the planet.

In this paper we use spectra with surface temperatures warm enough (> 220 K) to provide sufficient thermal contrast between the surface and atmosphere for the accurate retrieval of atmospheric opacities. This restricts coverage to daytime measurements. Spectra from both the periapsis pass (which was in daylight during aerobraking and science phasing) and the daytime portions of the apoapsis observations are used. When daytime periapsis and apoapsis data overlap spatially and are separated in time by less than a day, dust opacities between the two usually agree to within measurement error.

## 3. Dust Opacity Retrieval Algorithm

To retrieve dust opacity, we first compute the equivalent column-integrated opacity of pure absorbers as a function of wavenumber. Then, we estimate the contribution of dust to the total opacity by fitting predetermined spectral shapes (opacity as a function wavenumber) for dust, water ice, and the effect of a nonunit emissivity surface to the observed opacity spectrum.

### 3.1. Opacity Spectrum

If we neglect the small contributions from the solar beam and scattering from atmospheric aerosols, and assume a plane-parallel atmosphere, then the observed monochromatic radiance of Mars as a frequency of wavenumber, $I_{obs}(\nu)$, can be written as

$$I_{obs}(\nu) = \epsilon(\nu)\, B[T_{surf}, \nu]\, e^{-\tau_0(\nu)/\mu} + \int_0^{\tau_0(\nu)} B[T(\tau), \nu]\, e^{-\tau/\mu}\, d\tau. \quad (1)$$

where $\epsilon(\nu)$ is the surface emissivity at frequency $\nu$, $\tau_0$ is the normal column-integrated aerosol opacity, $\mu$ is

the cosine of the emission angle, $B[T, \nu]$ is the Planck function, $T_{\rm surf}$ is the surface temperature, $T(\tau)$ is the atmospheric temperature, and the integral is performed from the spacecraft (at $\tau = 0$) to the surface (at $\tau = \tau_0$).

The procedure used to retrieve column-integrated aerosol opacity is a numerical solution of (1) for $\tau_0(\nu)$. Input are the data (radiance at each wavenumber), a priori information in the form of a previously retrieved surface temperature and atmospheric temperature profile, and assumptions that the dust is well-mixed and nonscattering that are described in detail below. The expected radiance for a range of opacities ($\tau_0$) is computed using (1) until a pair of opacities is found that brackets the observed radiance. The opacity where the expected radiance matches the observed radiance is then found by standard root-finding techniques. This procedure is repeated for each wavenumber in the observed spectrum. The final solution is the spectral dependence of the equivalent column-integrated opacity of purely absorbing aerosols for a ray normal to the surface, $\tau_0(\nu)$.

To solve (1) for opacity, atmospheric and surface temperatures are required. Atmospheric temperatures were retrieved for each TES spectrum using a constrained linear inversion of radiances in the 15-$\mu$m $CO_2$ band (see the accompanying paper by *Conrath et al.* [this issue] for details). For this study the retrievals for temperature and aerosol opacity were performed sequentially (instead of simultaneously). In the temperature retrieval we have accounted for dust opacity to first order by using an effective surface temperature calculated by taking the brightness temperatures in narrow spectral intervals on either side of the $CO_2$ band and averaging them. The spectral intervals are 508–529 and 814–825 cm$^{-1}$. Temperatures from the surface to about 0.1 mbar (35 km) are obtained with a typical vertical resolution of about one scale height (10 km). Surface temperatures were obtained by using the brightness temperature in a small spectral window near 1300 cm$^{-1}$, where the brightness temperature is highest (see Figure 1).

We make two major simplifying assumptions to be able to numerically solve (1) for the equivalent column-integrated opacity $\tau_0$. First, we assume that atmospheric opacity sources (primarily dust and water ice) are well-mixed with the $CO_2$ gas. Obviously, this is not always the case. Using Viking orbiter images, *Jaquin et al.* [1986] observed vertical structure in dust hazes. However, analysis of limb scans from the Viking lander Sun diodes [*Pollack et al.*, 1977] and images from the Pathfinder lander [*Smith et al.*, 1997] indicates that at most times the well-mixed approximation is a good one. Furthermore, our experience with the TES data shows that dust opacity scales very well with both surface pressure and 1/cos(emission angle), both indicating that dust opacity is proportional to the amount of gas along the line of sight. Because well-mixed dust means that dust opacity along the line of sight is directly proportional to atmospheric pressure, the integration over $\tau$ in (1) can be changed to an integration over pressure. Atmospheric temperature $T(\tau)$ can then be replaced with $T(p)$, which is the quantity that is directly retrieved from the 15-$\mu$m $CO_2$ band.

The second assumption that we make is that the dust aerosols are nonscattering. Therefore we are retrieving an equivalent absorption dust opacity instead of the full extinction (absorption plus scattering) dust opacity. For nadir viewing geometry and the typical opacities found outside of dust storms of $\tau_0 \leq 0.25$, the effect of scattering is small, and the absorption dust opacity is very nearly equal to the extinction dust opacity. For the daytime spectra used here, the absorption dust opacity tends to be a slight underestimate (typically 10–20%) of the true extinction dust opacity. During the very dustiest times when opacities approach unity, scattering may become important, and in that case our dust opacity estimates become more of an indicator of relative dust opacity rather than an absolute measure of the amount of dust in the atmosphere.

### 3.2. Spectral Shape Fitting

In order to obtain an accurate dust opacity, it is important to account for the opacity contribution from water ice and from a nonunit emissivity surface, especially during times of relatively low dust opacity. Not including these contributions can lead to a substantial overestimation of dust opacity. A detailed description of this effect is given by *Smith et al.* [this issue]. To estimate the contributions of dust, water ice, and nonunit surface emissivity to the opacity spectrum found above, we assume that the opacity spectrum $\tau_0(\nu)$ can be described by

$$\tau_0(\nu) = A_{\rm dust}({\rm lat}, {\rm lon}) f_{\rm dust}(\nu) + A_{\rm ice}({\rm lat}, {\rm lon}) f_{\rm ice}(\nu) + A_{\rm surf}({\rm lat}, {\rm lon}) g_{\rm surf}(\nu) \frac{\partial \tau_0}{\partial \epsilon}, \quad (2)$$

where $f_{\rm dust}$ and $f_{\rm ice}$ are the spectral shapes (opacity as a function of wavenumber) of dust and water

ice aerosols, $g_{surf}$ is the spectral shape of the surface (one minus emissivity as a function of wavenumber), the $A$ parameters describe the horizontal (spectrum-to-spectrum) variation in the contribution from each component, and $\epsilon$ is surface emissivity.

For each opacity spectrum a least squares fit for $A_{dust}$, $A_{ice}$, and $A_{surf}$ is performed by assuming that the spectral shapes $f_{dust}$, $f_{ice}$, and $g_{surf}$ are fixed and known [see *Smith et al.*, this issue; *Bandfield et al.*, this issue]. The derivative term in (2) is computed numerically for each spectrum by varying surface emissivity in (1). Finally, a simple quality control is performed that excludes all fits with high residual and unphysical values for the $A$ parameters. The resulting best fit value for $A_{dust}$ is then the column-integrated opacity of dust at 1075 $cm^{-1}$ (since $f_{dust} = 1$ at 1075 $cm^{-1}$) and is the quantity for "dust opacity" that we use in the remainder of this paper.

In performing the least squares fit, we use the spectral shapes for dust and water ice opacity adopted by *Smith et al.* [this issue]. For the surface emissivity spectral shape we use that derived for orbit 219 (Cimmeria Terra) by *Smith et al.* [this issue], which has a broad feature from 850 to 1200 $cm^{-1}$ and an emissivity at 250–550 $cm^{-1}$ roughly equal to that at 1000–1100 $cm^{-1}$. Although the surface spectral shape has some similarity to the dust spectral shape at 850–1200 $cm^{-1}$, the opacity of dust is much reduced at 250–550 $cm^{-1}$ relative to the peak at 1075 $cm^{-1}$, while the surface emissivity has comparable values in the two spectral regions. Surface emissivity varies with location on the planet but is always > 0.90 at 1000 $cm^{-1}$.

### 3.3. Estimation of Uncertainties

Uncertainty in the retrieved value of dust opacity comes from instrument noise and calibration, errors in the surface temperature and atmospheric temperature, and the assumptions outlined above (fixed spectral shapes and a well-mixed vertical distribution for dust). Using a conservative (noisy) estimate for the instrument noise of $3 \times 10^{-8}$ W $cm^{-2}$ $sr^{-1}/cm^{-1}$ [*Christensen et al.*, 1992, 1998; *Christensen*, 1999] gives a typical dust opacity uncertainty of 0.02 for one spectral channel. However, because we fit spectral shapes over many frequencies, the uncertainty caused by noise is very small. Conservative estimates for the uncertainty in surface temperature (0.5 K) and in atmospheric temperatures (3 K) also give dust opacity uncertainties of 0.02 each. All of these uncertainties are inversely related to the amount of thermal contrast between the atmosphere and surface. Values quoted here are for a thermal contrast of 20–40 K, which is, again, conservative for the observations used in this study.

The uncertainty introduced by assuming fixed spectral shapes is much more difficult to quantify. *Bandfield et al.* [this issue] and *Smith et al.* [this issue] show that dust and water ice spectral shapes have only minor variations (< 5%) for the vast majority of spectra. The surface emissivity spectral shape may show more variation. There are certainly regions that display surface emissivities that are significantly different than the spectral shape computed over Cimmeria Terra on orbit 219 (for example, the region with strong hematite features described by *Christensen et al.* [this issue]. However, *Christensen* [1982, 1998] shows that the presence of surface emissivity spectral features is highly correlated with low-albedo regions and that although there are meaningful differences between surface emissivity spectra taken at different low-albedo locations, the general spectral shape of those surface emissivity spectra is broadly similar to the orbit 219 Cimmeria Terra spectrum. Furthermore, any surface emissivity that is significantly different than what we assumed here would cause a high residual in our fit and would be rejected by our quality control procedure. Thus, for the purpose of obtaining dust opacity, most surface emissivity spectral shapes computed thus far can be considered to be variations of the orbit 219 shape. We estimate that the uncertainty in dust opacity introduced by assuming a fixed surface emissivity spectral shape is no more than 0.03.

The uncertainty caused by dust not being well-mixed (dust layering) is also very difficult to estimate. However, as noted earlier, our experience with the data is that this effect is small and has negligible impact on the uncertainty calculation. Adding all these uncertainties together, assuming that they are uncorrelated, leads to a total uncertainty estimate of about 0.05 for any one dust opacity retrieval.

## 4. Results

The procedure described above yields ~330,000 individual retrievals of column-integrated dust opacity. The dust opacities presented below are given for 1075 $cm^{-1}$, which is at the peak of the dust absorption. The spectral dependence of dust is shown in Figure 2.

Figu
2

Because the approximation that dust is well-mixed with the $CO_2$ gas is quite good, the large topographic

variations on Mars make comparisons of dust opacity between one place and another difficult unless the topography is "removed" by scaling to a reference pressure. In the plates below we scale all dust opacities to an equivalent 6.1-mbar pressure. This scaling also corrects for the bias in opacities caused by the annual variation of surface pressure, which has an amplitude of about 20% [*Hess et al.*, 1980].

### 4.1. Overview

Plate 1 gives an overview of dust opacity as observed by TES. Dust opacities at 1075 $cm^{-1}$ scaled to an equivalent 6.1-mbar surface are given for seven different latitude bands. Dust opacity averages are obtained by first placing all the data from one orbit into bins 15° wide in latitude and 30° wide in longitude. Then, the dust opacity for each orbit and latitude band is obtained by averaging all longitude bins for that orbit and latitude that contain data. This two-step average is performed to minimize bias caused by uneven longitude coverage because TES takes approximately the same number of measurements near the longitude of periapsis as at all other longitudes combined.

When TES first began observations just after southern spring equinox, there was a general latitudinal gradient in dust opacity with higher opacities to the south. A moderate regional dust storm at mid-southern latitudes was observed at around $L_s$=190°. Throughout the period $L_s$=184°–220° there was increased dust activity at the edge of the retreating southern seasonal polar ice cap (see *Kieffer et al.* [this issue] for a detailed description of the recession of the south polar ice cap). During the period $L_s$=215°–225° there was a general trend of increasing dustiness in the southern hemisphere perhaps caused by the numerous local storms observed along the edge of the south polar ice cap. *Leovy et al.* [1973] postulated that local dust storms along the retreating southern polar ice cap would contribute to a background opacity in the southern hemisphere that could make conditions favorable for the initiation of large dust storms.

At $L_s$=225°, TES observed a very large regional dust storm which originated in the Noachis Terra region. Dust opacity increased at all latitudes and rapidly spread east and west over the course of the next week. However, it is clear from Plate 1 that the increase in dust opacity was far greater to the south of 30°S than in was to the north and that this large regional storm did not attain truly global status. The main body of the dust storm began to subside after a few sols, although significant activity remained throughout the rest of the aerobraking phase at high southerly latitudes (60°–75°S).

When the science-phasing orbit began at $L_s$=304°, the atmosphere was relatively clear. Shortly after that, at $L_s$=309°, TES observed a moderately large regional dust storm that originated north of the Argyre basin and spread to the south and east. The last part of the science-phasing orbit ($L_s$=0°–28°) was characterized by gradual clearing from a regional dust storm observed in microwave temperature soundings by *Clancy et al.* [this issue] at $L_s$=340°, punctuated by occasional small localized dust storms.

The variation of atmospheric temperature with time over this period (presented by *Conrath et al.* [this issue], Figure 2) shows correlations with the dust opacity trend. There are rapid increases of 10–15 K in atmospheric temperatures at the 0.3-mbar pressure level (about 30-km altitude) in both the northern and southern hemispheres associated with the larger dust storms mentioned above (the Noachis dust storm at $L_s$=225° and the regional dust storm at $L_s$=309°). The rapid and large amplitude response of the atmosphere in both hemispheres implies a strong interaction between dust opacity and the dynamical state of the atmosphere.

### 4.2. Noachis Dust Storm

The major dust event during these observations was the Noachis dust storm which began on November 26, 1997 ($L_s$=225°). Plate 2 shows a map incorporating each dust opacity measurement taken during the main part of the storm ($L_s$=225°–233°). The 12 strips of data running roughly north and south from 30°N to 30°S represent the periapsis passes from the 12 orbits used. The even distribution of observations at all longitudes southward of 30°S latitude comes from the apoapsis portion of the orbit. Our selection of data with a warm surface and a significant thermal contrast between the surface and atmosphere excludes observations taken over the polar ice cap, which at this time extended to about 68°S.

Plate 3 shows the evolution of the storm. The orbital period at this time was about 30 hours. The main core of the storm was located in Noachis Terra between 20°–55°S latitude and 330°–10°W longitude. During the storm, high dust opacities (> 0.5) spread to all longitudes poleward of 40°S. The storm preferentially spread to the south and east. The evolution of the storm is qualitatively similar to the regional dust storm modeled by *Murphy et al.* [1995, Figure

3] with expansion of the dust first poleward in direction and then quickly spreading to all longitudes at high southerly latitudes.

In the northern hemisphere, dust opacities were not significantly elevated above prestorm levels until orbit 53 ($L_s$=226°, approximately 4 sols after the beginning of the storm). Opacities remained elevated until at least orbit 57 ($L_s$=231°, 9 sols after the beginning of the storm) before a gradual clearing began. In the north, there was somewhat more dust opacity at longitudes near the storm center (330°–10°W) than in the opposite hemisphere (150°–190°W), but there was considerably less longitudinal structure than in the southern hemisphere. The sparse longitude coverage in the northern hemisphere for each orbit (data are primarily from periapsis passes only) limits detailed analysis of northern hemisphere data.

In the southern hemisphere, large changes in the intensity and areal extent of the dust storm were observed from orbit to orbit. The main core of the Noachis storm quickly intensified, reaching a maximum strength at about orbit 53 ($L_s$=226°, 4 sols after the beginning of the storm). At this time the main core covered the area from about 20°S latitude to at least the edge of the polar cap (68°S) and from 270°W longitude through the prime meridian to 60°W longitude. Large gradients in opacity existed in the growth phase of the dust storm with opacities at and exceeding unity inside the dust storm but still at nearly prestorm levels (0.3–0.4) just outside the dust storm. At the height of the Noachis dust storm, atmospheric temperatures inside the dust storm were 10–20 K warmer at the 0.3-mbar pressure level (about 30-km altitude) than they were at the same latitude outside the dust storm.

Over the next 4 to 5 sols the main core of the Noachis core began to slowly dissipate. However, dust continued to spread, and opacities of at least 0.5 covered all longitudes poleward of 40°S latitude by orbit 57 ($L_s$=231°, 9 sols after the beginning of the storm). By orbits 59 and 60 ($L_s$=233°, 12 sols after the beginning of the storm), the Noachis storm center was no longer well organized, and a new center of activity at 60°–70°S and 180°–270°W had established itself. The Noachis storm center dissipated by orbit 70 ($L_s$=241°, 25 sols after the beginning of the storm), but the satellite storm at 60°–70°S persisted for quite some time, maintaining a higher dust opacity than surrounding longitudes until about $L_s$=270° (see Plate 1). There was significantly more dust opacity at 180°–270°W longitude than at other longitudes. Although the Noachis storm center was gone by orbit 70, dust opacity levels throughout the southern hemisphere remained significantly higher than before the storm until the gradual clearing of the atmosphere brought them back down to prestorm levels at around $L_s$=270°.

By fitting the dust opacity trends in Plate 1 for the latitude bands 45°–60°S and 60°–75°S to an exponential function, we estimate an exponential decay constant of 49 sols for the main Noachis storm. The 30°–45°S latitude band has a decay constant of 75 sols, and the decay constant for more northerly latitude bands (far outside the core of the storm) is even longer.

### 4.3. Other Dust Storms

In addition to the Noachis and its satellite dust storm, TES observed several other significant dust storms. At $L_s$=309° a compact but intense dust storm started at 20°–50°S latitude, 20°–120°W longitude (the area north and northwest of Argyre). Plate 4 is a map showing all dust opacity measurements obtained during the storm ($L_s$=309°–319°). As the storm evolved it spread south and east forming a new core of activity at 65°–80°S latitude, 180°–270°W longitude that outlived the activity north of Argyre. In this way the evolution of the dust storm was remarkably similar to that of the Noachis dust storm. However, unlike the Noachis storm the $L_s$=309° storm had very little influence outside its core regions. As shown in Plate 4, dust opacity remained at low prestorm levels (0.15–0.20) at all latitudes north of 65°S between 150°–320°W longitude. Even in the longitude where the storm was most active (0°–120°W), there was no significant change in northern hemisphere dust opacities outside of a couple isolated local dust storms that were probably unrelated to the southern hemisphere regional storm.

A smaller and less intense regional dust storm was observed by TES at the beginning of our observations at $L_s$=184°. Plate 5 is a map showing all observations between $L_s$=184°–195°. There are two centers of increased dust opacity at southern midlatitudes. The main one was located at 40°–60°S latitude, 300°–340°W longitude (west of Hellas), and a smaller one was located at 40°–60°S latitude, 20°–50°W longitude (Argyre). The edge of the south polar ice cap was at about 60 S at this time. These two regions were active simultaneously, and both peaked in intensity near $L_s$=192°. Neither of these storms migrated.

Numerous smaller dust storms were also recorded

by TES, ranging in size from several hundreds of kilometers down to a single TES pixel (roughly 10 km). Many of these storms occurred at the edge of the retreating south polar seasonal ice cap. Few of these local storms had normalized dust opacities > 0.5, and none lasted for longer than a sol or two. Table 1 lists a few of the larger local dust storms.

### 4.4. Comparison With Other Spacecraft Missions

The Mariner 9 mission arrived at Mars in 1971 during the decay of perhaps the largest dust storm ever recorded [*Martin and Zurek*, 1993]. The Mariner 9 IRIS instrument [*Hanel et al.*, 1972a, b] took thermal infrared spectra similar to TES from $L_s$=293° to 352°, with an additional very few spectra between $L_s$=352° and 98°. This corresponds in season to TES data taken during the science-phasing orbit. *Fenton et al.* [1997] convolved IRIS spectra with the Viking IRTM spectral response functions and used the method of *Martin* [1986] to retrieve dust opacities. They found 9-$\mu$m opacities of 0.5–0.8 at the beginning of the mission soon after the peak of the great dust storm ($L_s$=293°–300°), with opacities decaying to about 0.2 after the dust storm had cleared ($L_s$=330°–340°). *Fenton et al.* [1997] computed exponential decay constants for the dust storm of 42 days (41 sols) at high southerly latitudes (55°–65°S) and 67 days (65 sols) at midsoutherly latitudes (20°–30°S). *Conrath* [1975] found a decay rate of 60 days (58 sols) for the 1971 storm based on 2-mbar temperatures. There was no global dust storm observed by TES during this season, but the "background" dust opacity of 0.2 is similar to that observed by TES (before the $L_s$=309° regional dust storm), and the decay constant for the 1971 global dust storm is comparable to that for the Noachis storm (49 sols in the core, 75 sols just to the north) observed by TES.

Mariner 9 dust opacities have also been retrieved by *Santee and Crisp* [1993], who performed a simultaneous retrieval of atmospheric temperatures and dust opacity on IRIS spectra taken between $L_s$=343° and 348° after the dust storm had cleared. They found 9-$\mu$m dust opacities of 0.25–0.3 near the equator and somewhat lower values (0.1–0.2) to the north and south. The variation by a factor of 2 in dust opacity with latitude is not observed by TES, but the overall median dust opacity reported by Santee and Crisp (0.2) is similar to that observed by TES.

Dust opacities were monitored by the Viking orbiters and landers for more than one Mars year (1976–1978). *Martin* [1986] and *Martin and Richardson* [1993] used data from the infrared thermal mapper (IRTM) instrument to retrieve 9-$\mu$m opacities, while *Pollack et al.* [1977, 1979] and *Colburn et al.* [1989] used observations of the Sun by the landers to retrieve dust opacities at visible wavelengths. TES measures infrared opacities, so the IRTM data set is the most directly comparable Viking observation. Comparison of infrared and visible dust opacities is more difficult because the ratio of dust opacity between the two wavelengths is not well known. We choose a conversion factor of 2.0 for the ratio of visible to 9-$\mu$m opacities based on the work of *Clancy et al.* [1995]. During the season observed by TES ($L_s$=184°–28°), Viking observed two global dust storms, each having opacities exceeding unity over a wide latitude range [*Martin*, 1986], with decay constants of 75 sols for the first storm and 51 sols for the second storm [*Pollack et al.*, 1979]. The Noachis dust storm observed by TES did not reach the size of the storms observed by Viking, but the decay constants for all three storms were similar.

Dust opacities observed at $L_s$=40° (well away from regional dust storms in both the Viking and Global Surveyor years) were 0.1–0.2 using Viking IRTM data [*Martin*, 1986], about 0.5 in the Viking optical data [*Colburn et al.*, 1989], and 0.1 for TES. Given the IRTM spectral response and the dust spectral shape from Figure 2, dust opacities from the IRTM should be 0.835 times as large as dust opacities reported here for TES. Therefore the equivalent IRTM dust opacity is 0.12–0.24. Given a measured surface pressure at the Viking Lander 1 site of about 8.3 mbar [*Hess et al.*, 1980], and using a conversion factor of 2.0 for the ratio of visible to 9-$\mu$m opacities [*Clancy et al.*, 1995], the equivalent Viking lander dust opacity becomes 0.18. Therefore TES dust opacity appears to be somewhat lower than the Viking opacities, although a new calibration of atmospheric temperatures derived by the IRTM (R. J. Wilson and M. I. Richardson, The Martian atmosphere during the Viking Mission, 1, Infrared measurements of atmospheric temperatures revisited, submitted to *Icarus*, 1999) may affect dust opacities derived from IRTM data. At $L_s$ = 200°, before the major Viking and Global Surveyor dust storms, dust opacities were about 0.4 (IRTM dust opacity from *Martin* [1986] converted to TES equivalent), 0.4 (Viking lander visible dust opacity from *Colburn et al.* [1989] converted to TES equivalent), and 0.15 from TES. TES observations imply that during this last Mars year, the southern spring and sum-

mer seasons were less dusty than the corresponding season during the first Viking year.

The Mars Pathfinder landed on the surface of Mars on July 4, 1997, and operated for 84 sols [*Golombek et al.*, 1997], corresponding to a seasonal range of $L_s$=142°–189°, during which a short period of overlap exists between TES and Pathfinder dust opacity measurements. *Smith et al.* [1997] used observations of the Sun by Pathfinder to obtain dust opacities at visible wavelengths. They found dust opacities gradually rising from about 0.45 at the beginning of the mission to 0.55 at the end. To convert to a TES equivalent dust opacity, we use a measured surface pressure of about 6.7 mbar at the Pathfinder landing site [*Schofield et al.*, 1997] and a conversion factor of 2.0 for the ratio of visible to 9-$\mu$m dust opacities [*Clancy et al.*, 1995]. The TES equivalent Pathfinder dust opacities are then 0.20–0.25. This is somewhat higher than the 0.15 measured by TES at the latitude of the Pathfinder (19°N) and that season.

## 5. Summary

Even before achieving its final mapping orbit, the Thermal Emission Spectrometer has already provided a very valuable data set by monitoring the Mars atmosphere for more than half a Mars year ($L_s$=184°–28°). During this period, TES observed one large regional dust storm (Noachis, at $L_s$=225°), three smaller (but still significant) regional dust storms ($L_s$=192°, 252°, and 309°), and numerous local dust storms. During southern spring and early summer when the south seasonal polar ice cap was retreating, there was consistently more activity (local dust storms) and a higher background dust opacity at high southerly latitudes near the edge of the ice cap than at other latitudes. Nominal dust opacities when there were no dust storms were about 0.15–0.2.

There was no global dust storm of the magnitude of those observed by Mariner 9 or Viking observed by TES, but the large, regional dust storm (Noachis) that was observed by TES was extensive, and it was recorded in unprecedented detail. Atmospheric temperatures and dust opacities were observed before, at the height, and during the decay of the Noachis storm without interruption. In the sols leading up to the Noachis dust storm, there was a significant and general rise in southern hemisphere dust opacity and in local dust storm activity. The Noachis dust storm spread and intensified to its maximum extent in about 10 sols, covering all longitudes poleward of 40°S latitude with significant dust opacity ($>$ 0.5). The dust storm then decayed with an exponential time constant of about 49 sols. A rapid temperature increase of 10–15 K at the 0.3-mbar pressure level was observed in both hemispheres [*Conrath et al.*, this issue] implying strong interaction between dust opacity and the dynamical state of the atmosphere.

There is significant and poorly understood interannual variability in dust opacities on Mars, especially in the strength and number of regional and global dust storms. The data set returned by TES during aerobraking and science phasing helps to extend the record of Mars dust observations and also gives us our best ever look at the detailed distribution and evolution of dust in the Mars atmosphere.

**Acknowledgments.** The authors wish to thank Monte Kaelberer, Karen Horrocks, Eric Winter, and Emily Greene for providing software development and data-handling expertise at Goddard Space Flight Center. We also thank the TES operations team at Arizona State University, including Kelly Bender, Noel Gorelick, and Greg Mehall. Josh Bandfield, Todd Clancy, Ted Roush, Conway Leovy, and an anonymous referee provided helpful comments on this manuscript. Finally, we thank the entire spacecraft and mission operations teams at the Jet Propulsion Lab and Lockheed Martin.

## References


Albee, A. L., F. D. Palluconi, and R. E. Arvidson, Mars Global Surveyor Mission: Overview and status, *Science, 279*, 1671–1672, 1998.

Bandfield, J. L., P. R. Christensen, and M. D. Smith, Spectral data set factor analysis and end-member recovery: Application to analysis of Martian atmospheric particulates, *J. Geophys. Res.*, this issue.

Beish, J. D., and D. C. Parker, Meteorological survey of Mars, 1969–1984. *J. Geophys. Res., 95*, 14,657–14,675, 1990.

Chase, S. C., Jr., J. L. Engel, H. W. Eyerly, H. H. Kieffer, F. D. Palluconi, and D. Schofield, Viking infrared thermal mapper. *Appl. Opt., 17*, 1243–1251, 1978.

Christensen, P. R., Martian dust mantling and surface composition: Interpretation of thermophysical properties. *J. Geophys. Res., 87*, 9985–9998, 1982.

Christensen, P. R., Variations in Martian surface composition and cloud occurrence determined from thermal infrared spectroscopy: Analysis of Viking and Mariner 9 data, *J. Geophys. Res., 103*, 1733–1746, 1998.

Christensen, P. R., Calibration report for the Thermal Emission Spectrometer (TES) for the Mars Global Surveyor Mission. Mars Global Surveyor Project, Jet Propul. Lab., Pasadena, Calif., 1999.

Christensen, P. R., et al., Thermal Emission Spectrometer Experiment: Mars Observer Mission, *J. Geophys. Res., 97*, 7719–7734, 1992.

Christensen, P. R., et al., Results from the Mars Global Surveyor Thermal Emission Spectrometer, *Science, 279*, 1692–1698, 1998.

Christensen, P. R., J. L. Bandfield, R. N. Clark, K. S. Edgett, V. E. Hamilton, T. Hoefen, H. H. Kieffer, R. O. Kuzmin, M. D. Lane, M. C. Malin, R. V. Morris, J. C. Pearl, R. Pearson, T. L. Roush, S. W. Ruff, and M. D. Smith, Detection of crystalline hematite mineralization on Mars by the Thermal Emission Spectrometer: Evidence for near-surface water, *J. Geophys. Res.*, this issue.

Cimino, G., and W. M. Calvin, Calibration and analysis of Mariner 7 infrared spectra, *Bull. Am. Astron. Soc., 28*, 1068, 1996.

Clancy, R. T., S. W. Lee, G. R. Gladstone, W. W. McMillan, and T. Roush, A new model for Mars atmospheric dust based upon analysis of ultraviolet through infrared observations from Mariner 9, Viking, and Phobos, *J. Geophys. Res., 100*, 5251–5263, 1995.

Clancy, R. T., B. J. Sandor, M. J. Wolff, P. R. Christensen, M. D. Smith, J. C. Pearl, B. J. Conrath, and R. J. Wilson, An intercomparison of ground-based millimeter, MGS TES, and Viking atmospheric temperature measurements: Seasonal and interannual variability of temperatures and dust loading in the global Mars atmosphere, *J. Geophys. Res.*, this issue.

Colburn, D. S., J. B. Pollack, and R. M. Haberle, Diurnal variations in optical depth at Mars, *Icarus, 79*, 159–189, 1989.

Conrath, B. J., Thermal structure of the Martian atmosphere during the dissipation of the dust storm of 1971, *Icarus, 24*, 36–46, 1975.

Conrath, B. J., J. C. Pearl, M. D. Smith, W. C. Maguire, S. Dason, M. S. Kaelberer, and P. R. Christensen, Mars Global Surveyor Thermal Emission Spectrometer (TES) observations: Atmospheric temperatures during aerobraking and science phasing, *J. Geophys. Res.*, this issue.

Curran, R. J., B. J. Conrath, R. A. Hanel, V. G. Kunde, and J. C. Pearl, Mars: Mariner 9 spectroscopic evidence for $H_2O$ ice clouds, *Science, 182*, 381–383, 1973.

Fenton, L. K., J. C. Pearl, and T. Z. Martin, Mapping Mariner 9 dust opacities, *Icarus, 130*, 115–124, 1997.

Golombek, M. P., et al., Overview of the Mars Pathfinder Mission and assessment of landing site predictions, *Science, 278*, 1743–1748, 1997.

Hanel, R. A., B. Schlachman, E. Breihan, R. Bywaters, F. Chapman, M. Rhodes, D. Rodgers, and D. Vanous, The Mariner 9 Michelson interferometer, *Appl. Opt., 11*, 2625–2634, 1972a.

Hanel, R. A., et al., Investigation of the Martian environment by infrared spectroscopy on Mariner 9, *Icarus, 17*, 423–442, 1972b.

Hess, S. L., J. A. Ryan, J. E. Tillman, R. M. Henry, and C. B. Leovy, The annual cycle of pressure on Mars measured by Viking Landers 1 and 2. *Geophys. Res. Lett., 7*, 197–200, 1980.

Horn, D., J. M. McAfee, A. M. Winer, D. C. Herr, and G. C. Pimentel, The composition of the Martian atmosphere: Minor constituents, *Icarus, 16*, 543–556, 1972.

Ivanov, A. B., and D. O. Muhleman, Opacity of the Martian atmosphere from the Mars Orbiter Laser Altimeter (MOLA) observations, *Geophys. Res. Lett., 25*, 4417–4420, 1998.

James, P. B., M. J. Wolff, S. W. Lee, R. T. Clancy, J. F. Bell III, and L. J. Martin, HST Observations of early Spring dust storms in the north polar region of Mars, *Bull. Am. Astron. Soc., 29*, 961, 1997.

Jaquin, F., P. G. Gierasch, and R. Kahn, The vertical structure of limb hazes in the Martian atmosphere, *Icarus, 68*, 442–461, 1986.

Kieffer, H. H., T. N. Titus, K. F. Mullins, and P. R. Christensen, Mars south polar spring and summer behavior observed by TES: Seasonal cap evolution controlled by frost grain size, *J. Geophys. Res.*, this issue.

Leovy, C. B., R. W. Zurek, and J. B. Pollack, Mechanisms for Mars dust storms, *J. Atmos. Sci., 30*, 749–762, 1973.

Malin, M. C., Mars Orbiter Camera: The first year, *Bull. Amer. Astron. Soc., 30*, 1020, 1998.

Malin, M. C., et al., Early views of the Martian surface from the Mars Orbiter Camera of Mars Global Surveyor, *Science, 279*, 1681–1685, 1998.

Martin, L. J., and R. W. Zurek, An analysis of the history

of dust activity on Mars, *J. Geophys. Res., 98*, 3221–3246, 1993.

Martin, T. Z., Thermal infrared opacity of the Martian atmosphere, *Icarus, 66*, 2–21, 1986.

Martin, T. Z., and M. I. Richardson, New dust opacity mapping from Viking infrared thermal mapper data, *J. Geophys. Res., 98*, 10,941-10,949, 1993.

Murphy, J. R., J. B. Pollack, R. M. Haberle, C. B. Leovy, O. B. Toon, and J. Schaeffer, Three-dimensional numerical simulation of Martian global dust storms, *J. Geophys. Res., 100*, 26,357–26,376, 1995.

Peterfreund, A. R., Contemporary aeolian processes on Mars: Local dust storms, Ph.D. thesis, Ariz. State Univ., Tempe, 1985.

Pollack, J. B., D. S. Colburn, R. Kahn, J. Hunter, W. Van Camp, C. E. Carlston, and M. R. Wolf, Properties of aerosols in the Martian atmosphere, as inferred from Viking lander imaging data, *J. Geophys. Res., 82*, 4479–4496, 1977.

Pollack, J. B., D. S. Colburn, F. M. Flasar, R. Kahn, C. E. Carlston, and D. Pidek, Properties and effects of dust particles suspended in the Martian atmosphere, *J. Geophys. Res., 84*, 2929–2945, 1979.

Pollack, J. B., T. Roush, F. Whitteborn, J. Bregman, D. Wooden, C. Stoker, O. B. Toon, D. Rank, B. Dalton, and R. Freedman, Thermal emission spectra of Mars (5.4–10.5 microns): Evidence for sulfates, carbonates, and hydrates, *J. Geophys. Res., 95*, 14595–14628, 1990.

Roush, T., J. B. Pollack, F. Whitteborn, J. Bell III, and B. Sitton, Thermal infrared spectroscopic observations of Mars from the Kuiper Airborne Observatory (KAO): Constraints on past climates and weathering products, in *Airborne Astronomy Symposium on the Galactic Ecosystem: From Gas to Stars to Dust, Astron. Soc. Pac. Conf. Ser.*, vol. 73, edited by H. Haas, J. Davidson, and E. Erickson, pp. 345–348. Astron. Soc. of the Pac., San Francisco, Calif., 1995.

Santee, M., and D. Crisp, Thermal structure and dust loading of the Martian atmosphere during late southern summer: Mariner 9 revisited, *J. Geophys. Res., 98*, 3261–3279, 1993.

Schofield, J. T., J. R. Barnes, D. Crisp, R. M. Haberle, S. Larsen, J. A. Magalhães, J. R. Murphy, A. Seiff, and G. Wilson, The Mars Pathfinder Atmospheric Structure Investigation/Meteorology (ASI/MET) experiment, *Science, 278*, 1752–1758, 1997.

Smith, M. D., J. L. Bandfield, and P. R. Christensen, Separation of atmospheric and surface spectral features in Mars Global Surveyor Thermal Emission Spectrometer (TES) spectra, *J. Geophys. Res.*, this issue.

Smith, P. H., and M. Lemmon, Opacity of the Martian atmosphere measured by the Imager for Mars Pathfinder, *J. Geophys. Res., 104*, 8975–8985, 1999.

Smith, P. H., et al., Results from the Mars Pathfinder Camera, *Science, 278*, 1758–1765, 1997.

Toigo, A. D., A. P. Ingersoll, and B. C. Murray, Dust in the Martian atmosphere inferred from shadows in MOC images, *Eos Trans. AGU, 79 (17)*, Spring Meet. Suppl., S192, 1998.

Toon, O. B., and J. B. Pollack, Physical properties of the particles, composing the Martian dust storm of 1971–1972, *Icarus, 30*, 663–696, 1977.

Wolff, M. J., S. W. Lee, R. T. Clancy, L. J. Martin, J. F. Bell III, and P. B. James, 1995 observations of Martian dust storms using the Hubble Space Telescope, *J. Geophys. Res., 102*, 1679–1692, 1997.

P. R. Christensen, Department of Geology, Arizona State University, Tempe, AZ 85287.

B. J. Conrath, Center for Radiophysics and Space Research, Cornell University, Ithaca, NY 14853.

J. C. Pearl and M. D. Smith, NASA Goddard Space Flight Center, Code 693, Greenbelt, MD 20771. (Michael.D.Smith.1@gsfc.nasa.gov)

Received May 28, 1999; revised September 16, 1999; accepted September 27, 1999.

This preprint was prepared with AGU's LaTeX macros v5.01. File TES'Dust formatted March 20, 2000.

**Figure 1.** Examples of typical daytime Thermal Emission Spectrometer (TES) spectra. Radiances are shown in terms of equivalent brightness temperature to emphasize features. The signature of $CO_2$ gas, $H_2O$ ice aerosols, and dust aerosols are all easily identified and are distinct from each other. The uppermost curve shows a hot, midday spectrum with nominal dust opacity (0.2). The two lower curves show a spectrum taken at the height of the Noachis dust storm and a spectrum taken on the flank of Arsia Mons where there were a thick $H_2O$ cloud and low dust opacity due to the high elevation.

**Figure 2.** The spectral dependence of dust opacity (solid line) normalized to unity at 1075 $cm^{-}1$. Opacities are not computed in the spectral region where $CO_2$ has significant opacity (560–770 $cm^{-1}$).

**Plate 1.** Summary of column-integrated dust opacities observed by TES. Opacities are at 1075 $cm^{-1}$ and have been normalized to an equivalent 6.1 mbar surface. Regional dust storms are apparent at $L_s$=190°, 225°, and 309°.

**Plate 2.** Map showing all retrieved dust opacities taken during the main part of the Noachis dust storm ($L_s$=225°–233°). The storm began in the Noachis Terra region around 20°–50°S latitude, 320°–360°W longitude. No quantitative opacities were obtained at latitudes poleward of 68°S (over the polar cap). The color scale for this and the remaining plates represents dust opacity 0.2 as blue, 0.4 as green, and 0.75 or higher as red. Spot size is unrelated to the actual footprint size, which ranged from 10 km at periapsis to about 500 km for many of the high southerly observations taken in the apoapsis portion of the orbit.

**Plate 3.** Orbit-by-orbit evolution of the Noachis dust storm. The orbital period at this time was about 30 hours. Large orbit-to-orbit changes in the spatial extent and intensity of the storm were observed. The storm preferentially spread to the south and east. The center of activity at 60°–70°S and 180°–240°W persisted for quite some time after the main center in Noachis had largely subsided.

**Plate 4.** Map showing all retrieved dust opacities taken during the regional dust storm that occurred during science-phasing orbit ($L_s$=309°–319°). The storm was nearly as intense as the Noachis storm but was much more confined spatially.

**Plate 5.** Map showing all retrieved dust opacities taken during the regional dust storm that occurred at the beginning of the mission ($L_s$=184°–195°). Two centers of activity are seen near Hellas and Argyre, along with a general increase in dust opacity along the edge of the retreating south polar seasonal ice cap.

**Table 1.** Significant Local Dust Storms Observed by TES

| $L_s$, deg | Location | Comments |
|---|---|---|
| 205 | 25°S, 295°W | small; observed in only one orbit |
| 208 | 40–60°S, 170–200°W | small; observed in two orbits |
| 219 | 40–60°S, 100–180°W | beginning of numerous widespread small storms along cap edge |
| 224 | 45°S, 130°W | simultaneous with birth of Noachis storm; observed in only one spectrum |
| 236 | 30°N, 135°W | high opacity for north hemisphere |
| 252 | 35–45°S, 130–170°W | large, intense storm but gone quickly |
| 257 | 70°S, 350–360°W | small; beginning of much activity at high southerly latitudes |
| 258 | 70–75°S, 165–210°W | related to Noachis satellite? intense and lasted several orbits |
| 261 | 70–80°S, 250–290°W | spread east and intensified |
| 267 | 70–80°S, 190–230°W | intensification there part of a general dustiness at high southerly latitudes |
| 304 | 20°N, 45°W | near Viking 1 lander; also observed with the MGS MOC camera |
| 0 | 20–30°S, 330–360°W | late in the season; died away quickly |
| 3 | 40–50°S, 40–60°W | late in the season; died away quickly |

TOP

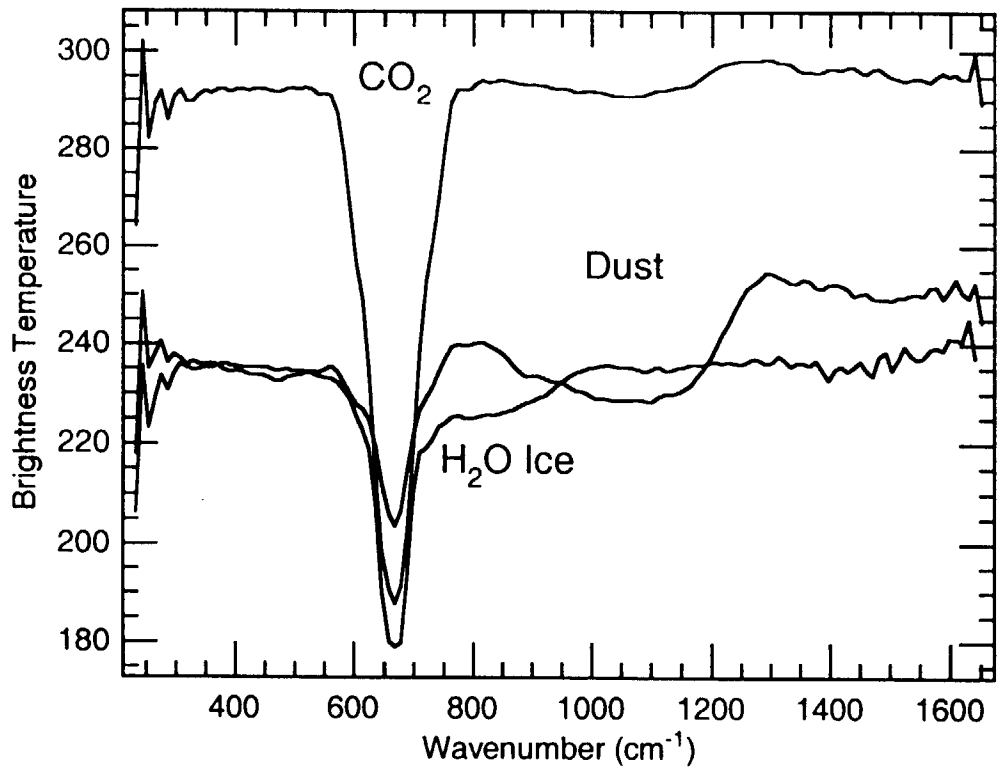


SMITH ET AL.
1999JE001097
FIG. 1

↑ TOP

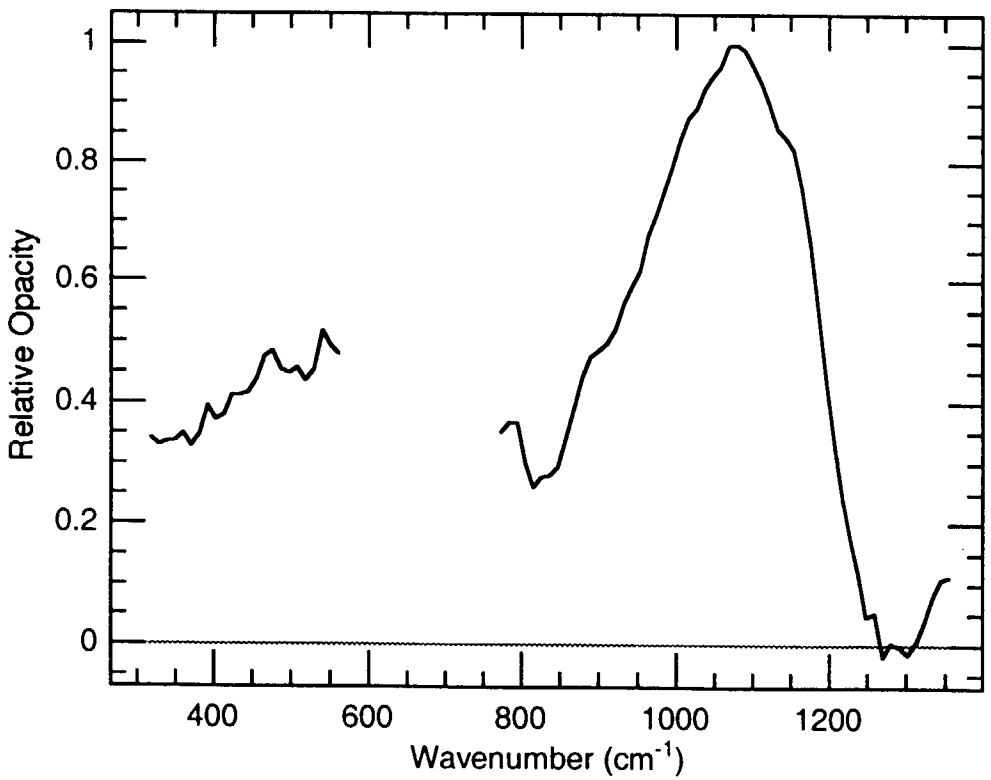


SMITH ET AL.
1999JE001097
FIG. 2

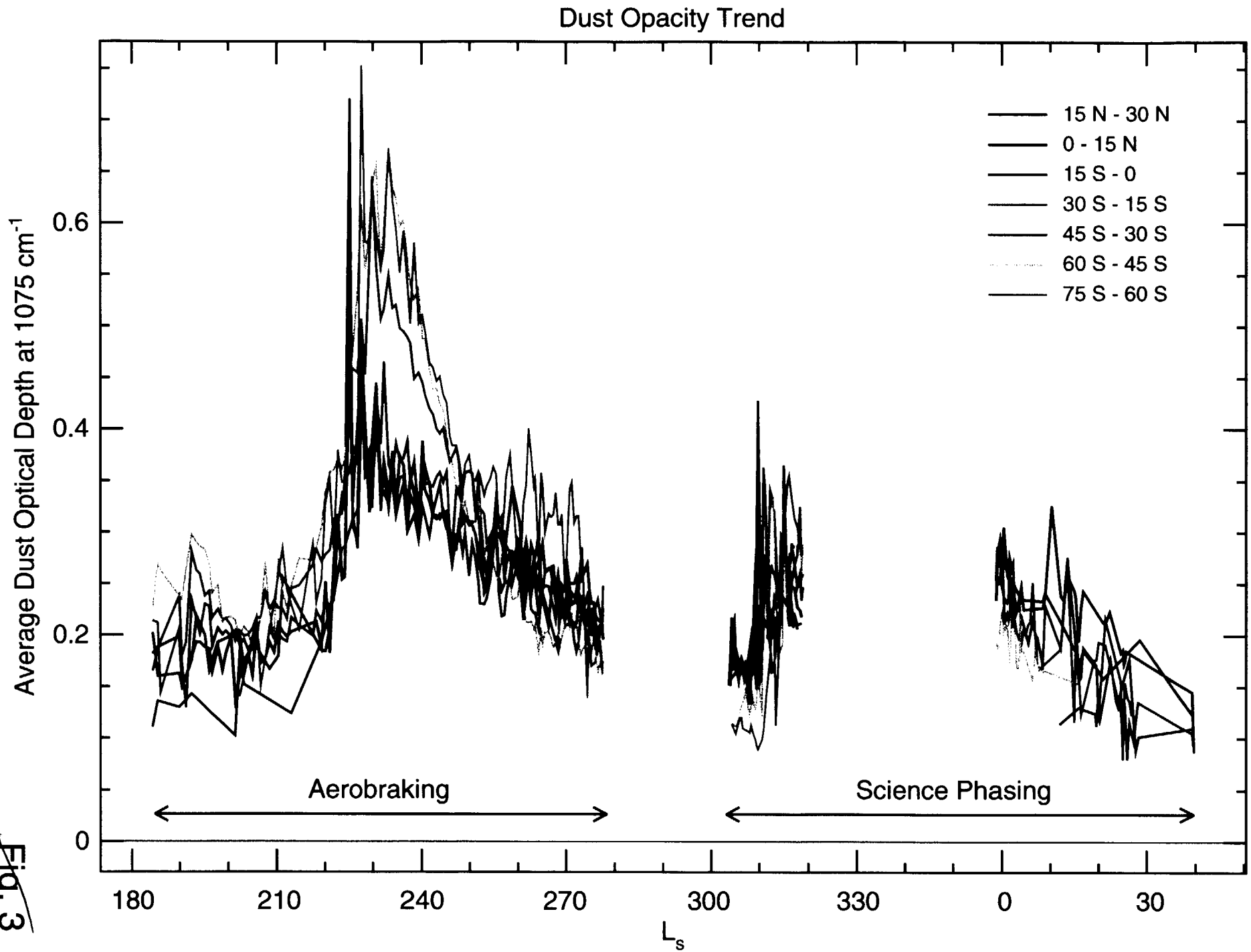
Dust Opacity Trend
15 N - 30 N
0 - 15 N
15 S - 0
30 S - 15 S
45 S - 30 S
60 S - 45 S
75 S - 60 S
Average Dust Optical Depth at 1075 cm-1
0
0.2
0.4
0.6
Aerobraking
Science Phasing
180
210
240
270
300
330
0
30
Ls

Fig. 3
Table 1

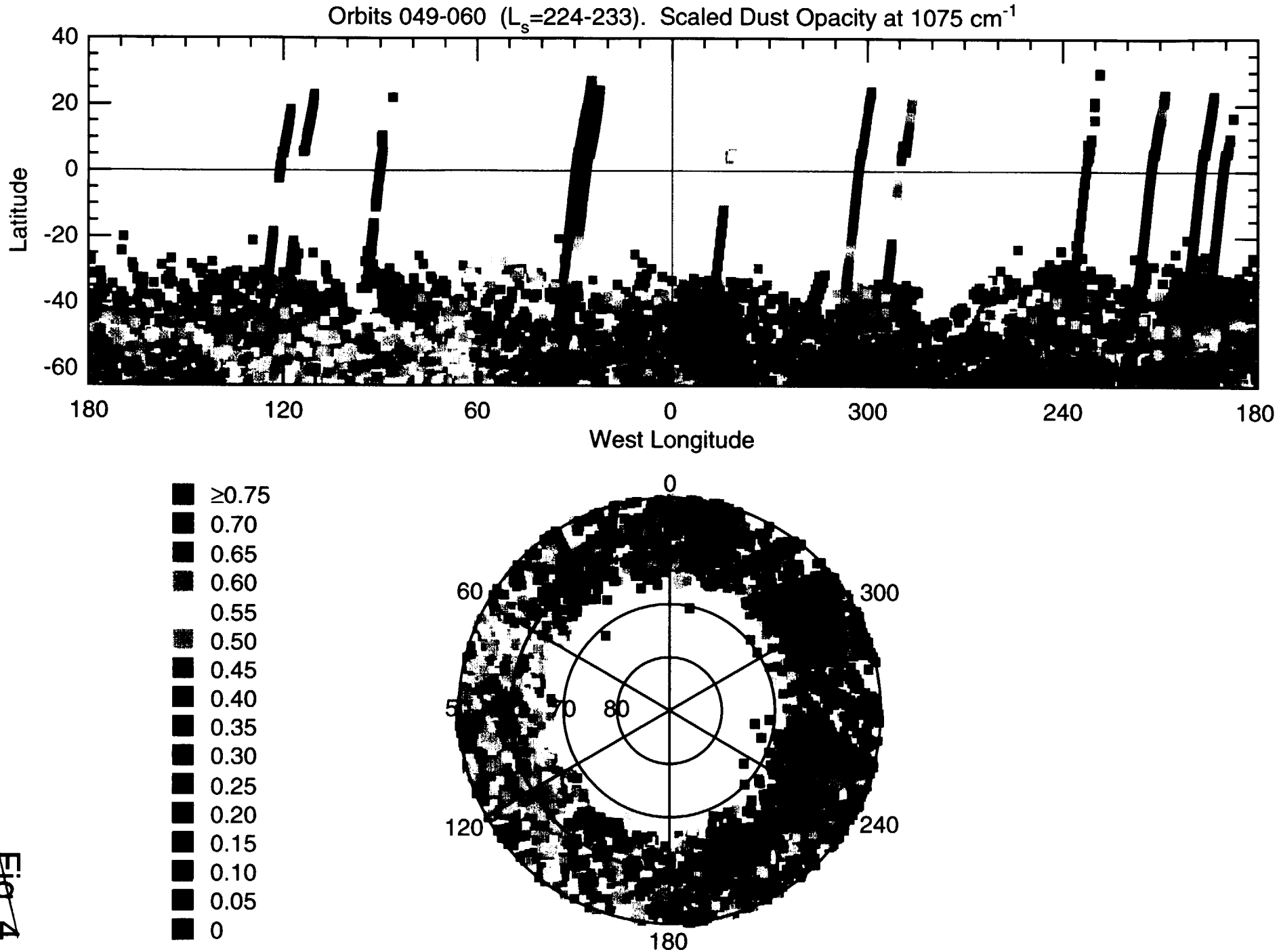
Orbits 049-060 ($L_s$=224-233). Scaled Dust Opacity at 1075 $cm^{-1}$
Latitude
40
20
0
-20
-40
-60
180
120
60
0
300
240
180
West Longitude
≥0.75
0.70
0.65
0.60
0.55
0.50
0.45
0.40
0.35
0.30
0.25
0.20
0.15
0.10
0.05
0
0
60
300
120
240
180

Fig. 4

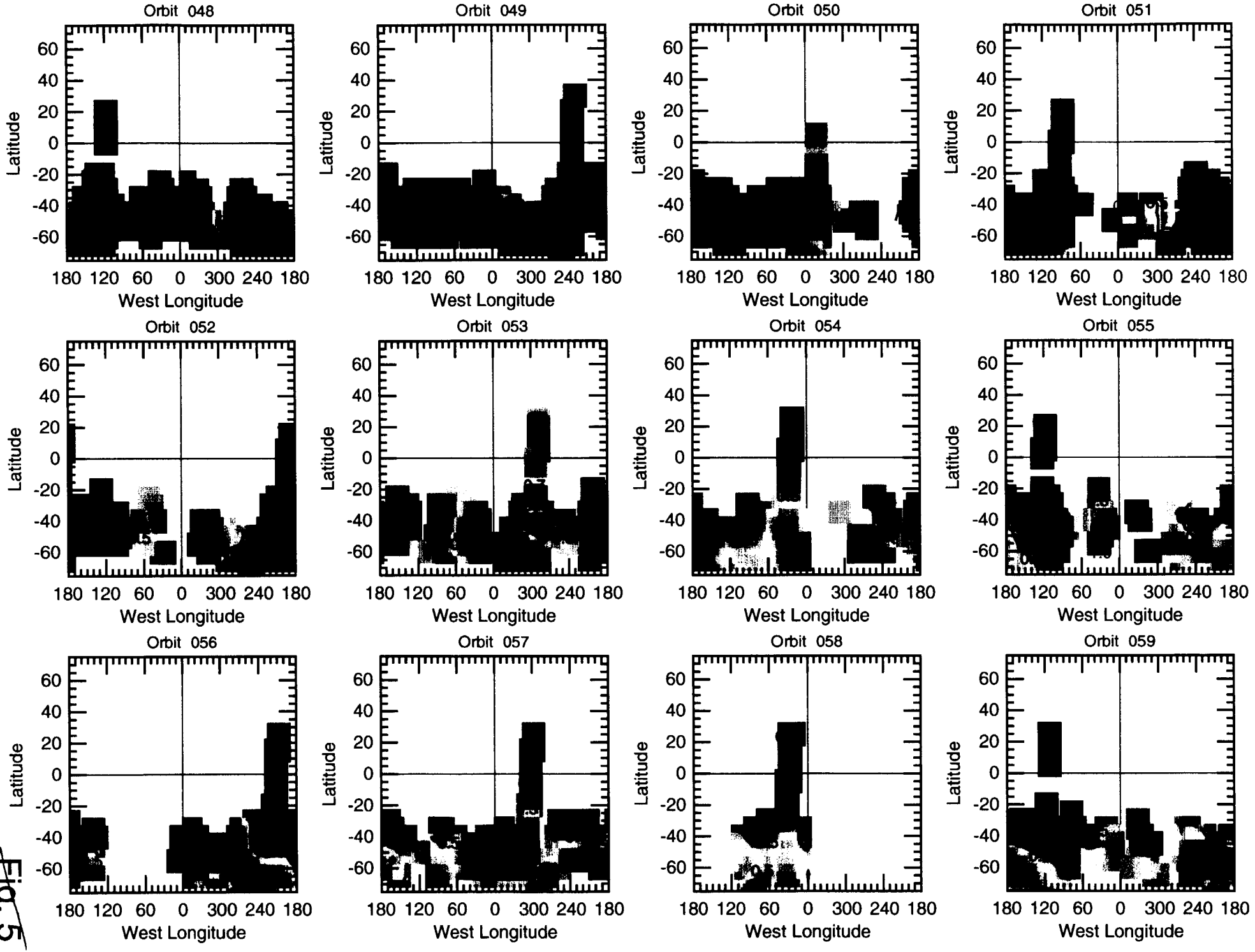
Orbit 048
Orbit 049
Orbit 050
Orbit 051
Orbit 052
Orbit 053
Orbit 054
Orbit 055
Orbit 056
Orbit 057
Orbit 058
Orbit 059
Latitude
60
40
20
0
-20
-40
-60
180 120 60 0 300 240 180
West Longitude

Fig. 5

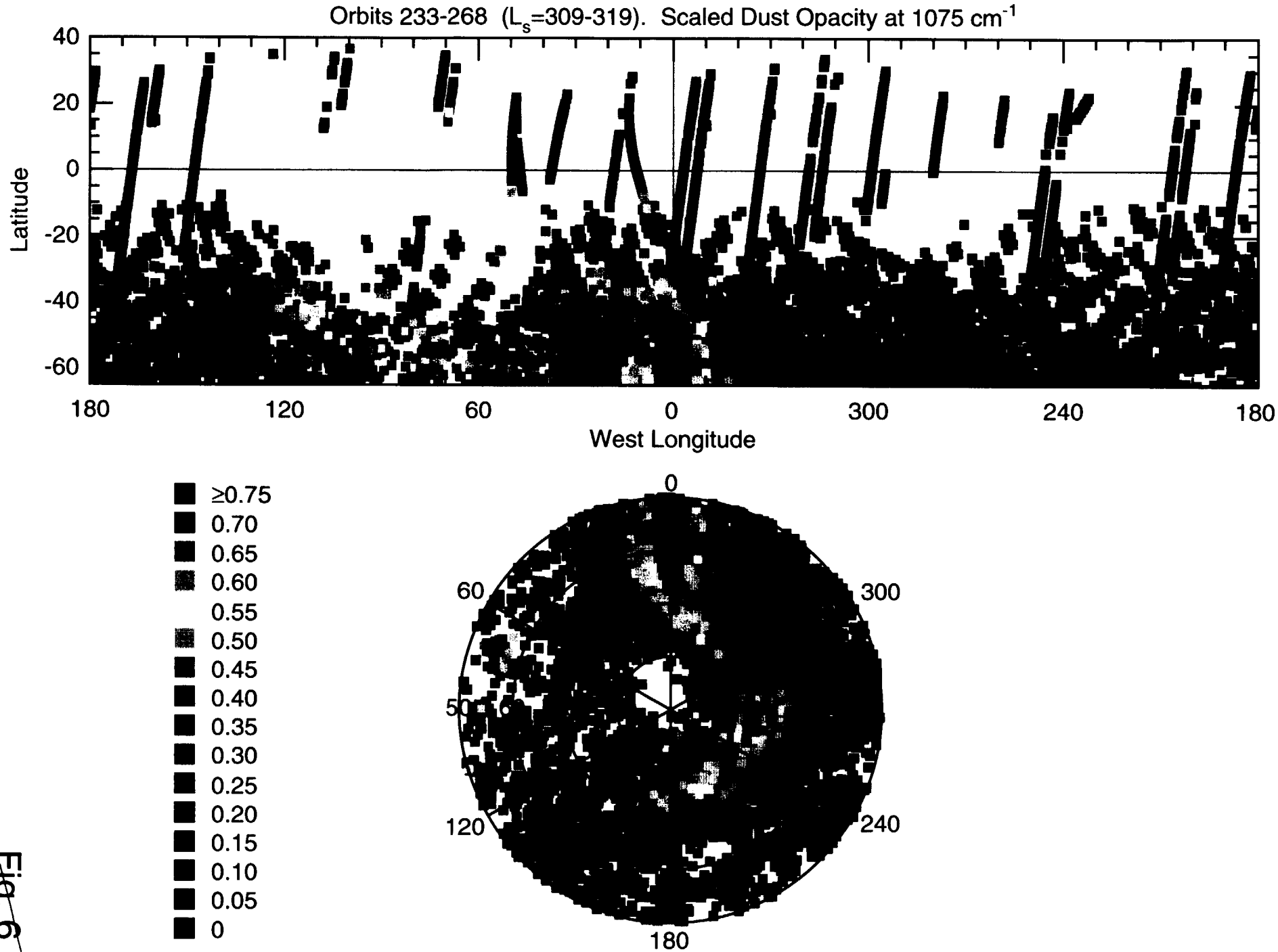
Orbits 233-268 ($L_s$=309-319). Scaled Dust Opacity at 1075 $cm^{-1}$
Latitude
40
20
0
-20
-40
-60
180
120
60
0
300
240
180
West Longitude
≥0.75
0.70
0.65
0.60
0.55
0.50
0.45
0.40
0.35
0.30
0.25
0.20
0.15
0.10
0.05
0
0
60
300
120
240
180

Fig. 6
Plate 4

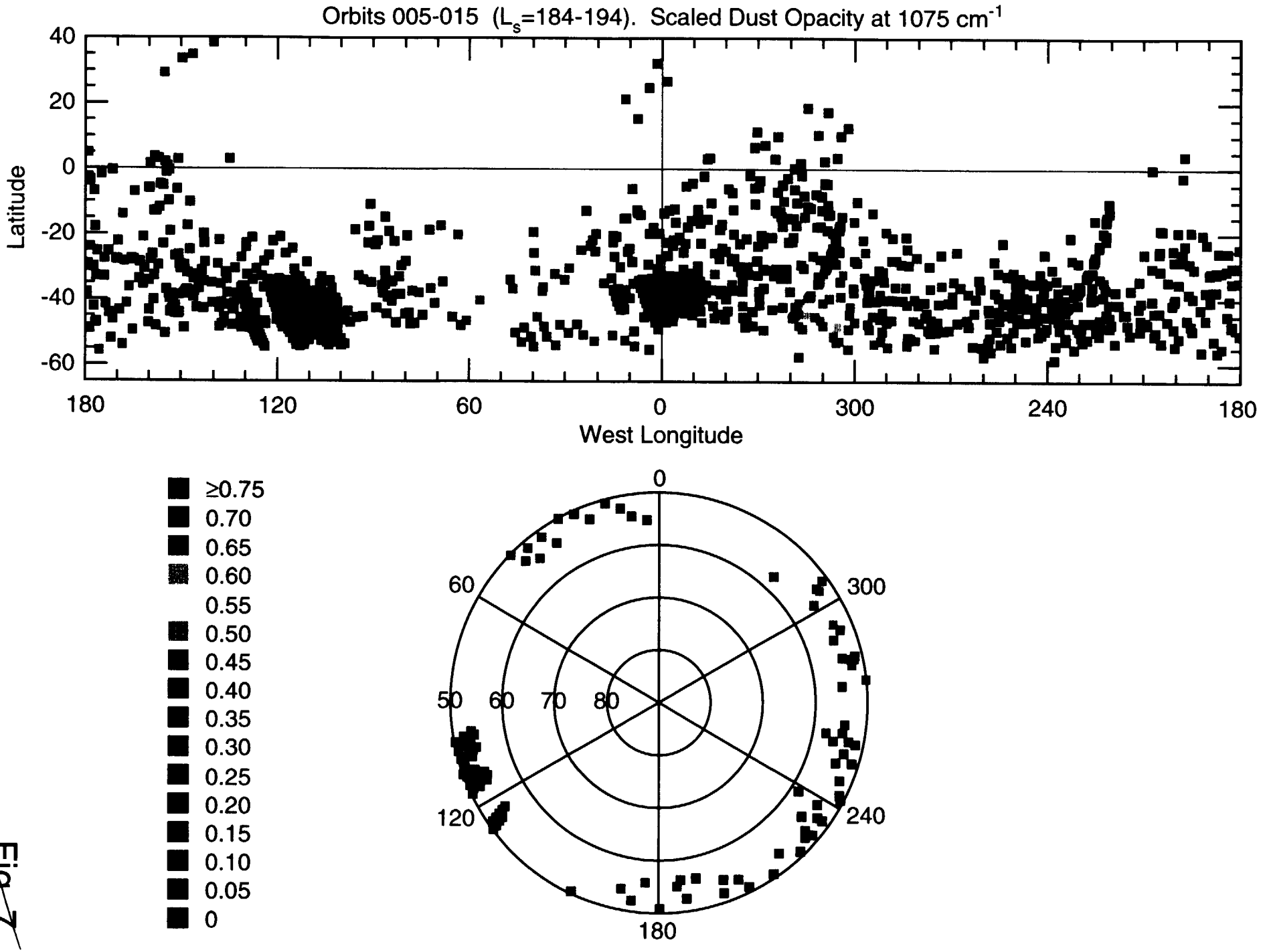
Orbits 005-015 ($L_s$=184-194). Scaled Dust Opacity at 1075 cm$^{-1}$
Latitude
40
20
0
-20
-40
-60
180
120
60
0
300
240
180
West Longitude
≥0.75
0.70
0.65
0.60
0.55
0.50
0.45
0.40
0.35
0.30
0.25
0.20
0.15
0.10
0.05
0
0
60
300
50
60
70
80
120
240
180

Fig. 7 plate 5